Density functional theory calculations of thermodynamic and kinetic properties of point defects in β-U

D. A. Andersson[a,*], C. Matthews[a], Y. Zhang[b], B. Beeler[c]

[a] *Materials Science and Technology Division, Los Alamos National Laboratory P.O. Box 1663, Los Alamos, NM 87545, USA*
[b] *University of Wisconsin*
[c] *Nuclear Materials, Computational Materials Science, North Carolina State University, Raleigh, NC, 27695, USA*

Abstract

Density functional theory (DFT) calculations of the thermodynamic and kinetic properties of point defects in the β phase of uranium ~~is~~ reported. Defect energies and entropies were calculated using $2 \times 2 \times 2$ supercells and the Generalized Gradient Approximation (GGA) of Perdew-Burke-Ernzerhof (PBE) for the exchange-correlation potential. Due to computational cost, calculations of the vibrational properties governing entropies were performed by only displacing atoms within (roughly) the 4th nearest neighbor shell of the defect, which implicitly assumes that atoms beyond this distance are unaffected by the defect. Migration barriers were estimated by nudged elastic band (NEB) calculations. The low symmetry of the β-U phase (the unit cell is tetragonal and contains 30 atoms) results in many point defect configurations and even more migration pathways. A connectivity map, starting from the most stable point defects, was developed in order to identify the rate-limiting step controlling the net diffusion rate in each crystallographic direction. The uranium self-diffusivity tensor was calculated by combining the defect formation energies, entropies, migration barriers and attempt frequencies. The fastest diffusion rate refers to a vacancy mechanism in the z crystallographic direction. The predicted uranium self-diffusivity for this mechanism agrees well with available experimental data. The diffusion mechanisms and rates identified in this study will inform fuel performance models of swelling and gas evolution.

1. Introduction

Metallic nuclear fuels are considered for application in several different reactor types, including micro-reactors and sodium-cooled fast reactors. Diffusion of point defects and fission gas atoms are important mechanisms for metal fuel microstructure evolution under irradiation and impact several fuel performance metrics, most importantly swelling. Uranium metal fuel, which is often alloyed with other elements such as Zr, Mo and/or Pu, exhibits several different stable phases as function of the radial position in the fuel rod. This is a consequence of the redistribution of alloying elements and the temperature gradient across the fuel rod that occurs for in-pile conditions. For accurate prediction of swelling, fission gas release, and other related processes, the diffusion properties of point defects and fission gas atoms must be determined for each phase of uranium in the fuel. The present study focuses on point defect properties and the resulting self-diffusion behavior in the β phase of uranium under thermal equilibrium conditions.

Self-diffusion in uranium has been investigated for the α-U [1], β-U [2] and γ-U [3] phases by isotope tracer diffusion experiments. The self-diffusivities differ by up to two orders of magnitude between the phases (from the β to the γ phase close to the phase transition temperature), even when the effect of temperature is accounted for by extrapolation, see Figure 1. The diffusivity correlates with the complexity of the crystal structure, with the ~~bcc~~ γ-U phase having much higher diffusivity than the more complex α and β phases. Although there is experimental data for self-diffusion in all three ura-

*Corresponding author. Present address: Materials Science and Technology Division, Los Alamos National Laboratory, MS G755, Los Alamos, NM 87545, USA, Tel: +1 505 665 8621

Email address: andersson@lanl.gov (D. A. Andersson)

nium phases, simulations are able to provide additional information, for example, in the form of separate defect formation and migration properties, the sum of which makes up the experimentally measured activation energy for self-diffusion, and the diffusivity of competing mechanisms that may become important under irradiation. The formation and migration terms are needed separately in order to accurately model the irradiation response of the fuel. Formation energies can be measured independently of the activation energies by positron annihilation spectroscopy, which has been reported in [4, 5] for γ-U (although raw positron data was presented for all phases, the defect formation energy was only reported for γ-U). The formation energies from positron annihilation spectroscopy can be used in combination with self-diffusion measurements of the activation energies to extract the migration barriers and thus enable direct comparison with the calculated values of the two separate contributions to the activation energy for self-diffusion. There are also other techniques to determine defect concentrations, e.g. dilatometry, and migration barriers, e.g. damage recovery experiments, but, to the best of our knowledge, no results have been reported using such techniques for uranium.

The bulk properties of the three main uranium phases have been studied using calculations and simulations based on both density functional theory (DFT) and empirical potentials [6–17]. The properties are well reproduced by the standard Generalized Gradient Approximation (GGA) exchange-correlation potential, and the application of a Hubbard U model to treat strong correlations among the 5f electrons is not required for metallic uranium [11–13]. There are also a number of computational investigations of the thermodynamic and kinetic properties of point defects. The formation and migration energies (no entropies) of point defects in the α-U phase were studied using DFT calculations in [6], which obtained an activation energy for diffusion in good agreement with experiments by Stelly and Servent [1] and Adda et al. [2]. The γ-U phase has been investigated using both static DFT calculations [9, 17] and ab initio molecular dynamics (AIMD) simulations [8]. Because γ-U is dynamically unstable at low temperatures, calculations are required to either utilize finite temperature (AIMD) [8] or methods to stabilize the bcc lattice for static 0 K DFT [9, 14–17], in order to avoid the lattice instability. AIMD simulations constitute the most rigorous approach, but they are also computationally very expensive. The calculated and measured diffusivities for γ-U differ by one or two orders of magnitude depending on temperature and the activation energies are slightly different between theory and experiments. The calculated vacancy formation energy is in good agreement with that measured by positron annihilation spectroscopy [4], suggesting that the slight deviation originates from the migration energy. Similar to the study of point defects in α-U, entropy contributions were neglected for γ-U. However, this simplification is not believed to contribute to significant uncertainty in either case.

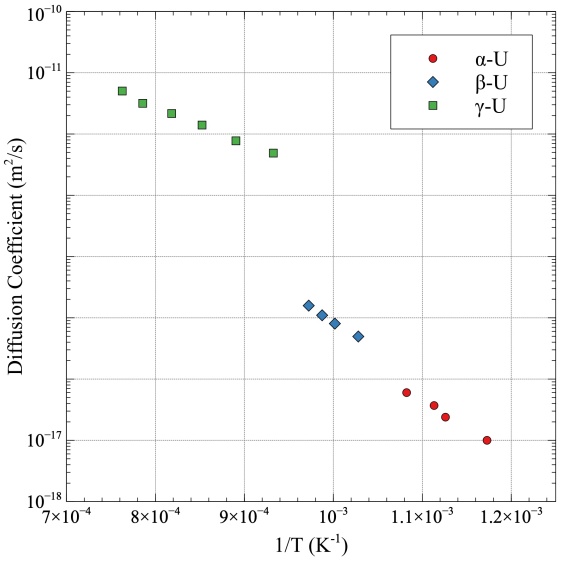

Figure 1: Collection of experimental data on self-diffusion in uranium phases as a function of inverse temperature. The data points are from [3] (γ), [18] (β) and [19] (α).

The β-U phase is stable in a narrow temperature range between the α-U and γ-U phases (943 K to 1048 K). There are a few computational studies of bulk β-U properties, which predicted lattice parameters in fairly good agreement with experiments [7, 20], although the high-temperature nature of the β-U phase complicates a one-to-one comparison with 0 K DFT calculations. Elastic constants were also calculated in [7], but, unfortunately, there is no experimental data to compare with.

Extending beyond bulk properties to defects, the present study reports results for the point defect thermodynamic and kinetic properties in the β-U phase utilizing DFT calculations. The lowest energy defect configurations are identified, migration energies of potential pathways are calculated, and a connectivity map derived from plausible path-

ways is constructed to estimate the effective diffusion rate in each crystallographic direction. The predictions are compared to available experimental data on uranium self-diffusion. The paper is organized as follows: First, the DFT methodology and the models used for predicting defect concentrations and self-diffusivities are presented; followed by the corresponding results, comparison to experimental data, discussion, and conclusions.

2. Computational methodology

2.1. DFT calculations

The point defect formation energies, entropies, migration barriers and attempt frequencies were calculated based on DFT using the VASP code [21–23]. Following the approach established in several existing DFT studies of uranium [13, 24], the exchange correlation potential was described by the Perdew-Burke-Ernzerhof (PBE) parametrization [25] of GGA without any Hubbard U parameter for the uranium 5f electrons or spin-polarization, as those are not necessary to reproduce the bulk properties of uranium. The projector augmented wave (PAW) method was used to describe the electrons [26, 27], with the 5d and 4f electrons treated as valance states. The softer version of the two available PAW potentials for uranium was applied. The predicted lattice parameters of the β phase are consistent with experimental data, which was already reported by others [7, 20], and summarized in Table 1. The discrepancies with regards to the $a = b$ lattice parameters are at least partially related to thermal expansion (the experimental data is ~~in the~~ high-temperature ~~region~~, more precisely 993 K, where the β phase is stable). It is unknown if this explanation pertains to the internal parameters as well. The finite temperature behavior of the uranium lattice could be investigated by performing AIMD simulations for β-U, but that is beyond the scope of the present study. Rather, it is assumed that the β-U description by DFT at 0 K is sufficiently representative of the high-temperature structure to extract defect and diffusion parameters. The tetragonal unit cell of β-U has low symmetry and contains 30 atoms (see Figure 2) [28], which gives rise to many point defect possibilities and even more migration pathways for vacancies and interstitials. The defect energies are calculated for all crystallographically unique uranium vacancies and for the most probable interstitial lattice positions. The results identify the lowest energy configurations. In order to obtain estimates of the effective diffusion rate in each crystallographic direction, a connectivity map starting from the most stable point defects was developed. The map is based on probable pathways informed by the calculated migration barriers.

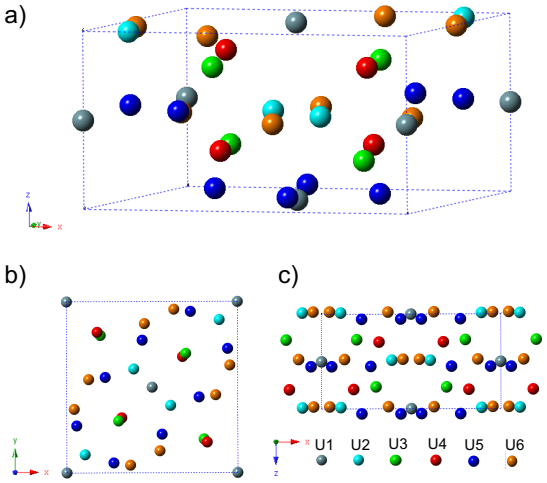

Figure 2: a) Unit cell of β-U with each unique crystallographic site (six) shown in different colors. Grey spheres correspond to the U1 position, turquoise to U2, green to U3, red to U4, blue to U5 and orange to U6. The supercells of β-U used in the present study are created by repeating this cell once in each crystallographic direction ($2\times2\times2$). b) The unit cell viewed in the z direction. c) The unit cell viewed in the y direction.

A 240 atom supercell consisting of $2 \times 2 \times 2$ unit cells ~~were~~ used to model the defect energies and migration barriers in β-U. The atomic positions, supercell volume, and supercell shape were allowed to fully relax (zero pressure on the cell and zero forces on the ions) in the energy minimization calculations. The calculations of migration barriers were performed at constant volume with the volume initially fixed at that of bulk β-U. For the rate-limiting step of the fastest diffusion mechanism, the results were further refined to include volume relaxation. The convergence criteria for the force relaxation was 0.01 eV/Å for all standard total energy calculations, but tighter convergence criteria (10^{-7} or 10^{-8} eV/Å) were applied for phonons. The plane-wave cut-off energy was set to 209.2 eV, which corresponds to the standard option for the accurate calculation setting in VASP. The total energy was calculated by integration in reciprocal space on $2\times2\times4$ Monkhorst-Pack k-point meshes [29] for the $2\times2\times2$

	$a = b$ (Å)	c (Å)	U1	U2	U3	U4	U5	U6
Calc.	10.438	5.687	0.0	0.109	0.323	0.322	0.557	0.360
			0.0	0.109	0.323	0.322	0.223	0.048
			0.518	0.0497	0.738	0.284	0.032	0.019
Calc. [7]	10.454	5.634						
Calc. [20]	10.520	5.707						
Exp. [28]	10.759	5.656	0.0	0.107	0.303	0.321	0.558	0.372
			0.0	0.107	0.303	0.321	0.225	0.045
			0.5	-0.014	0.769	0.294	0.052	-0.023

Table 1: Calculated crystallographic data for the β-U phase compared with experimental data [28] and DFT studies [7, 20]. The U1, etc., parameters represent the unique crystallographic positions in fractional coordinates.

supercells and the partial occupancies were smeared according to the Methfessel-Paxton method with a smearing width of 0.1 eV. The calculations for the β-U unit cell parameters, summarized in Table 1, used a $4\times4\times8$ Monkhorst-Pack k-point mesh, with all other settings being the same as for the supercell calculations. The phonon calculations applied a reduced $1\times1\times2$ k-point mesh for computational efficiency.

2.2. Defect and diffusion models

The thermodynamic and kinetic behavior of point defects were modeled based on a point defect model for defect concentrations and an Arrhenius model for the rate of defect migration, which combined gives the self-diffusivity of uranium.

Defect concentrations (fractional) are estimated from defect formation energies and entropies according to the dilute limit mass action law:

$$c_i = \exp\left(\frac{S_f^i}{k_B}\right)\exp\left(-\frac{E_f^i}{k_BT}\right), \tag{1}$$

where i denotes the defect, E_f^i and S_f^i are the defect formation energy and entropy, respectively, k_B is the Boltzmann constant and T is the temperature. This expression refers to the fraction of defects on a particular crystallographic site. The concentration per uranium atom, which is the quantity governing self-diffusion (see below), is obtained by weighting by the fraction of a particular site in relation to the total number of uranium atoms. This quantity is denoted c_α and the resulting defect concentration per uranium atom is obtained as $\tilde{c}_i = c_\alpha c_i$. The defect formation energies in Eq. 1 are calculated according to:

$$E_f^{V_U} = E(V_U) - E(U)\frac{N-1}{N} \tag{2}$$

and

$$E_f^{U_i} = E(U_i) - E(U)\frac{N+1}{N}, \tag{3}$$

where $E_f^{V_U}$ and $E_f^{U_i}$ are the vacancy and interstitial defect formation energies, respectively, $E(V_U)$ and $E(U_i)$ are the energies of a supercell with one vacancy and interstitial, respectively, $E(U)$ is the energy of the perfect supercell and N is the number of atoms in the supercell.

Defect formation entropies were calculated by assuming that the vibrational properties of atoms are only (significantly) affected by the defects inside (roughly) the 4th nearest neighbor shell or less (about 6 Å), an approach which was tailored to reduce the computational cost associated with displacing all the 240 atoms in the $2\times2\times2$ supercell. Table 2 summarizes the number of atoms in the affected set for each defect. The equivalence of Eq. 2 and 3 for entropies applied to the affected set of atoms is given by:

$$S_f^{V_U} = \tilde{S}(V_U) - \tilde{S}(U) + \frac{S(U)}{N} \tag{4}$$

$$S_f^{U_i} = \tilde{S}(U_i) - \tilde{S}(U) - \frac{S(U)}{N} \tag{5}$$

where $\tilde{S}(V_U)$ and $\tilde{S}(U_i)$ are the entropies of a supercell with one vacancy and interstitial (the $\tilde{S}$ denotes that these entropies are obtained from displacing the affected set of atoms), respectively, $S(U)$ is the entropy of the β-U supercell (obtained by displacing all atoms) and N the number of atoms in the supercell. The perfect cell vibrational defect entropy was calculated from the normal mode phonon frequencies following the approach of Mishin et al. [30]. At temperatures higher than the Debye temperature, the entropy of crystalline solids can be

approximated as:

$$S = -k_B \sum_{n=1}^{3N-3} \ln\left(\frac{\nu_n}{k_B T}\right) + (3N-3)k_B \qquad (6)$$

Here, N is the number of atoms in the crystal, k_B is the Boltzmann constant, T is the temperature, and ν_n is the normal vibrational frequency of the crystal. There are three modes that have imaginary frequencies for every supercell, corresponding to translational modes, which are neglected. The $\tilde{S}(V_U)$, $\tilde{S}(U_i)$ and $\tilde{S}(U)$ entropies are calculated using an equation similar to Eq. 6, but where the summation only covers the affected set of atoms for each case. The perfect cell summation adds the vacant site to the set for vacancies and the interstitial atom is removed for interstitials. In the harmonic approximation, the temperature dependence in Eq. 6 cancels for the formation entropies in Eqs. 4 and 5. The normal modes are calculated via the finite displacement method with a central difference scheme using VASP for the force calculations. Note that only the Γ point phonon frequencies are included in the evaluation of the entropy.

	V_{U1}	V_{U2}	V_{U3}	V_{U4}	V_{U5}	V_{U6}
#	21	16	17	10	12	18
	U_{i1}	U_{i2}	U_{i3}	U_{i4}	U_{i5}	U_{i6}
#	17	13	19	19	23	14

Table 2: Number of atoms included in the affected set of atoms for each defect (#). The total number of atoms in the cell is 239 for vacancies and 241 for interstitials.

The point defect diffusivities are obtained by combining a pre-exponential factor with an exponential containing the migration barrier in an Arrhenius expression :

$$D^i = D_0^i \exp\left(-\frac{E_m^i}{k_B T}\right). \qquad (7)$$

Migration barriers (E_m^i) were calculated using the nudged elastic band (NEB) method [24] with five images. The NEB calculations were performed with the volume fixed at that of bulk β-U. The diffusion mechanisms were identified by enumerating viable pathways, performing NEB calculations and then refining the pathways for cases where alternative options emerged. This approach is subject to the limitations of our ability to identify all important options and there is always a chance that a mechanism was missed. As such, the predicted diffusion coefficients represent a lower bound. For the rate-limiting step of the fastest diffusion mechanism, volume relaxation was performed with respect to the initial configuration and the climbing image version of the nudged elastic band method was used with five images [31]. The change in the migration barrier was small, < 0.02 eV, and consequently the fixed volume results without the climbing image method is considered sufficient for the purpose of screening viable diffusion pathways.

The pre-exponential factor for diffusion is given by:

$$D_0 = \frac{1}{D_z} f Z d^2 \nu, \qquad (8)$$

where ν is the attempt frequency for migration, d is the jump distance, Z is the number of available jump sites, f is the the correlation factor and D_z is the dimensionality of the diffusion mechanism (2 for 1D, 4 for 2D and 6 for 3D). The attempt frequency for migration can be calculated from the normal frequencies at the saddle point and at the initial configuration of the defect using the Vineyard method [32]:

$$\nu = \frac{\prod_{n=1}^{3N-3} \nu_n^{defect}}{\prod_{n=1}^{3N-4} \nu_n^{saddle}}. \qquad (9)$$

N is the number of atoms and imaginary frequencies are not included in the summation (three translational modes for the defect and the same three translational modes for the saddle point with an extra imaginary mode inherent to the nature of the saddle point). As an approximation, all attempt frequencies are initially set to $6.3 \times 10^{12} \mathrm{s}^{-1}$, which was calculated for the rate limiting self-diffusion step (see Sec. 3). ~~This~~ attempt frequency was calculated following the approach involving a reduced set of affected atoms outlined above. Frequencies arising from all other atoms are assumed to be the same for the initial configuration ~~as for~~ the saddle point, which is a necessary assumption to avoid excessive computational cost, while still allowing determination of frequencies with sufficient accuracy for the present purpose. The correlation factor is approximated as 1 in order to obtain an upper bound, which is slightly higher than the 0.781 value for the fcc lattice. Both d and Z are unique for each diffusion jump and dictated by the crystal structure (see Sec. 3.2.3).

The point defect diffusivities in Eq. 7 can be translated to self-diffusivities by accounting for the concentration of each defect per uranium atom.

The uranium self-diffusivity ascribed to a specific defect i is then obtained as

$$D_U^i = \tilde{c}_i D_0^i \exp\left(-\frac{E_m^i}{k_B T}\right). \quad (10)$$

The total diffusivity is obtained by summing up the contributions from all mechanisms. However, if one mechanism is dominant, the total diffusivity can safely be approximated by this mechanism alone. The concentration, $\tilde{c}_i$, refers to a specific site used as reference (starting point) for the diffusion mechanism (see Sec. 3 for further details). The migration barrier and the attempt frequency (entropy contribution) should be measured with respect to the same reference state, although the attempt frequency or entropy is only approximated for most mechanisms in the present study. As long as a consistent reference is used, any site along a diffusion pathway could be used as the starting point. The diffusivity is a tensor property and each tensor component must be evaluated separately. The tetragonal crystal structure of β-U means that there are two distinct crystallographic diffusion rates, here labeled as the in-plane x-y diffusivity and the z axis diffusivity. The diffusivity in polycrystalline materials can then be estimated by using known bounds or performing meso-scale simulations of textures of interest. Such an exercise is beyond the present scope.

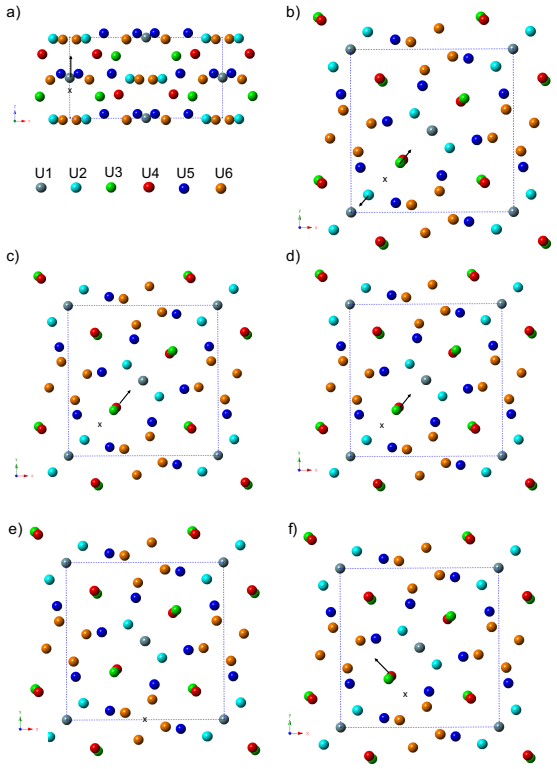

Figure 3: a)-f) Schematic illustration of interstitial positions 1 through 6 (U_{i1} through U_{i6}) in the β-U structure. The cell is expanded beyond the unit cell in order to capture the surrounding coordination. The fully relaxed structure files are available in the supplementary materials, which differ slightly from the schematics shown here. The interstitial atom is indicated by 'x' and surrounding atoms that experience significant displacement (split structures) are shown by arrows.

3. Results and discussion

3.1. Vacancy and interstitial formation energies and entropies

The calculated vacancy and interstitial formation energies and entropies are compiled in Table 3. The vacancy sites are labeled according to the uranium crystallographic site of the missing atom (V_{U1} for a vacant U1 site), see Figure 2, while the interstitial structures are shown in Figure 3. The defect concentrations obtained from the data in Table 3 using Eq. 1 are plotted in Figure 4. The vacancy of type 1 (V_{U1}) and interstitial of type 1 (U_{i1}) are shown to dominate across the entire temperature range relevant for the β-U phase. The stability of V_{U1} is driven by a high entropy contribution, since the formation energy of V_{U5} and V_{U6} are both lower than for V_{U1}. The high formation entropy may be related to the coordination environment, as U1 exhibits the longest distance to the nearest neighbor site among all crystallographic sites and the void created by the vacancy has the largest volume.

The formation energies and entropies of the most favorable vacancy and interstitial are collected in Table 4, which also includes the calculated reference values for α-U [1] and γ-U [2]. For γ-U, available experimental reference values are also reproduced [4, 5]. The vacancy formation energy is predicted to be higher in β-U than in α-U or γ-U. This is a consequence of V_{U1} dominating over V_{U5} and V_{U6} due to entropy contributions. V_{U5} and V_{U6} have formation energies close to that predicted for the γ-U phase. The interstitial formation energy for the β-U phase is in-between that of the α-U and γ-U phases, with the latter being significantly higher. The lowest energy interstitial structure forms a split interstitial in the z crystallographic direction. One of the vacancies (V_{U4}) and two of the interstitials have

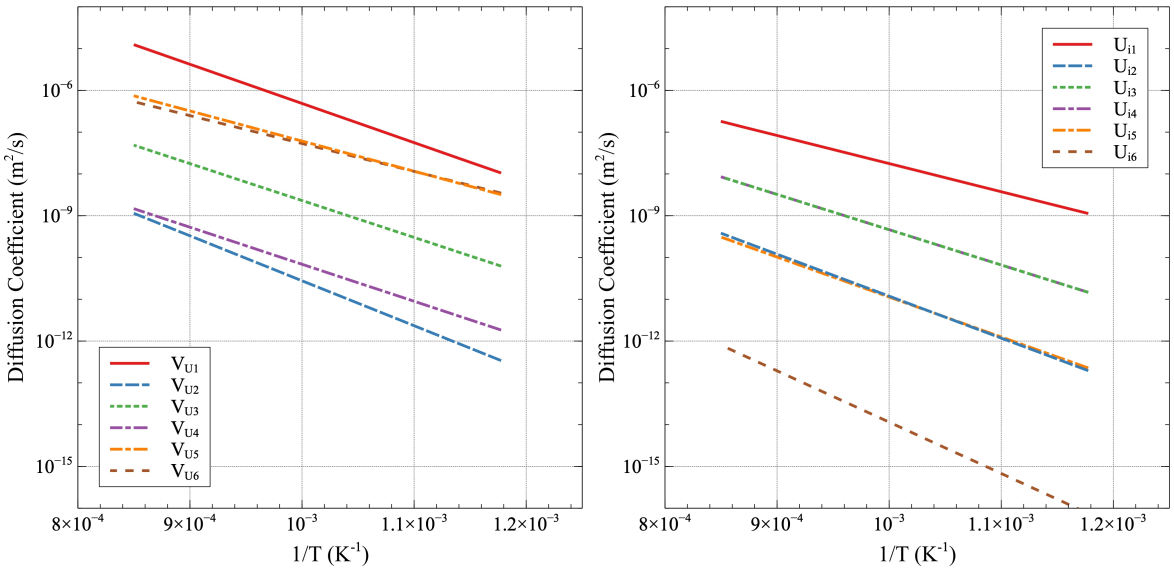

Figure 4: Predicted concentrations of a) vacancies and b) interstitials in β-U.

negative formation entropies (U_{i5} and U_{i6}). Negative formation entropies are not unphysical, but still somewhat unexpected and a sign of an unfavorable atomic coordination. None of the cases with negative formation entropies are very stable and further investigation of the origin is consequently curtailed. U_{i3} and U_{i4} relaxed to the same structure and are consequently assigned the same energy and entropy. Vacancies are predicted to be more abundant than interstitials in β-U.

	V_{U1}	V_{U2}	V_{U3}	V_{U4}	V_{U5}	V_{U6}
E_f	1.86	2.13	1.75	1.75	1.43	1.32
S_f	9.76	3.16	3.16	-0.28	2.71	1.34
	U_{i1}	U_{i2}	U_{i3}*	U_{i4}*	U_{i5}	U_{i6}
E_f	1.49	2.14	1.82	1.82	2.07	2.61
S_f	0.35	0.67	0.64	0.64	-0.49	-1.10

Table 3: Defect formation energies (E_f, eV) and entropies (S_f, k_B) for vacancies and interstitials at different crystallographic sites in β-U. The vacancy sites are based on the lattice location of uranium, see Figure 2, while the interstitial structures are shown in Figure 3. U_{i3} and U_{i4} (marked by an asterisk) relaxed to the same structure.

3.2. Defect migration mechanisms and barriers

Due to the low-symmetry of the β-U crystal structure, diffusion is complicated and net transport must inherently involve several steps. As an example, in order for a U1 vacancy to contribute to net diffusion, it must reach an equivalent site one lattice distance away, see Figure 5. This implies that it must jump through several other uranium sites. In order to estimate the effective migration barrier, the barriers of all intermediary steps and energies for each equilibrium lattice positions, must be calculated to identify the highest migration barrier (as measured from a common reference state) along a particular pathway. Among a range of different pathway options, the rate-controlling one will be that with the lowest effective migration barrier, however, just to re-iterate, it is the highest barrier along that pathway that ultimately controls the diffusion rate. Below the vacancy and interstitial diffusion mechanisms are reviewed and the relevant migration barriers reported.

3.2.1. Vacancy migration

The most probable in-plane (x-y) and out-of-plane (z) vacancy diffusion mechanisms are illustrated in Figure 5. Each step along the net diffusion pathways is shown with an arrow and the number next to it is the barrier in reference to the energy of a U6 vacancy (because it has the lowest formation energy, although the entropy ultimately favors the U1 vacancy). For in-plane x-y diffusion, the vacancy of type 1 is used as starting point, but any of the sites along a pathway could be considered as the starting position with a corresponding adjustment

	E_f [eV] (U_i)	S_f [k_B] (U_i)	E_f [eV] (V_U)	S_f [k_B] (V_U)
α-U [6] (Calc.)	4.14		1.69	
β-U [present work] (Calc.)	1.49	0.35	1.86	9.76
$\gamma - U$ [8] (1000 K) (Calc.)	0.37		1.34	
γ-U [4] (Exp.)			1.2 ± 0.25	
γ-U [5] (Exp.)			1.6 ± 0.16	

Table 4: Defect formation energies and entropies for vacancies and interstitials in the α, β and γ uranium phases. The β-U values refer to the most abundant type of vacancy and interstitial, see Fig. 4 and Table 3. The γ-U values are temperature dependent [8], but for the sake of simplicity we picked a fixed value at 1000 K for our analysis.

of the formation energy and migration barrier. The figure illustrates three main options for in-plane diffusion, with effective barriers ranging from 0.94 eV to 1.81 eV. There are additional permutations of the diffusion pathways shown in Figure 5, but they all reduce to the same effective barriers as those already shown. This implies that the effective barrier for diffusion in the x-y plane is 0.94 eV. The mechanism involves V_{U1}, V_{U2}, V_{U5}, V_{U6}, but sidesteps V_{U3} and V_{U4}. All the vacancy sites are covered by at least one of the three V_{U1} diffusion mechanisms. The enumeration in the figure suggests that all relevant pathways for diffusion in the x-y plane have been exhausted. Several additional calculations were performed in search of alternatives, but no transitions were found with barriers as low as those reported in Figure 6. Note that some of the x-y plane mechanisms also have a z component.

The four main alternatives for vacancy diffusion along the z axis are shown in Figure 6. Other pathways exist, but they were not included in the figure due to high barriers or the existence of more likely and shorter migration steps. The active diffusion mechanism has a low barrier of 0.27 eV (again with a U6 vacancy as the refererence) and involves the V_{U4} and V_{U6} vacancies, which is much lower than the barrier for diffusion in the x-y plane. Other mechanisms have barriers that are similar to the x-y plane diffusion mechanisms.

The effective migration barrier and other diffusion parameters for the active x-y and z diffusion mechanisms are collected in Table 5.

3.2.2. Interstitial migration

U_{i1} is the most stable interstitial configuration. Diffusion in the x-y plane occurs according to the mechanism in Figure 6. U_{i1} forms a split structure along the z axis with a U1 atom. Any of the two split atoms may diffuse by an interstitialcy mechanism where a U2 atom is kicked out to form a split interstitial with a U3 or U4 atom. The barrier and energy of the final state for the split structure involving U3 or U4 atoms are identical for all practical purposes. The diffusion step is completed by the split structure involving the U3/U4 atoms moving into a position similar to the starting position of a split interstitial involving a U1 atom. This step does not involve a U2 atom as in the first migration step. Finally, net diffusion occurs by repeating the multi-step mechanism just described in either the same or reverse order to complete migration through the unit cell. The effective barrier for this diffusion mechanism is 0.75 eV, which corresponds to moving the first split interstitial structure to the split structure involving the U3/U4 atom by way of a U2 atom. The same mechanism may lead to diffusion along the z axis by changing the direction of some of the jumps along z axis, as also illustrated in Figure 6. The net diffusion barrier is the same as for diffusion in the x-y plane. The effective migration barriers and other diffusion parameters of interstitials are summarized in Table 5.

3.2.3. Point defect diffusivities and uranium self-diffusivities

Based on the mechanisms identified in Secs. 3.2.1 and 3.2.2, the point defect diffusivities can be calculated from Eq. 7, with D_0 given by Eq. 8. The corresponding parameters are collected in Table 5 for the active vacancy and interstitial diffusion mechanisms in the x-y plane and along the z direction. The jump distances (d) are based on the distances to traverse the rate limiting barrier once, as derived from the pathways in Figures 5 and 6 (for net diffusion, the rate-limiting barrier has to be traversed twice, which cuts the effective diffusion ~~distancing~~ in half compared to the distance associated with completing a full diffusion step). The correlation factor (f) is set to one and we use $Z = 4$ for the x-y plane and 2 for the z axis. The fact that there

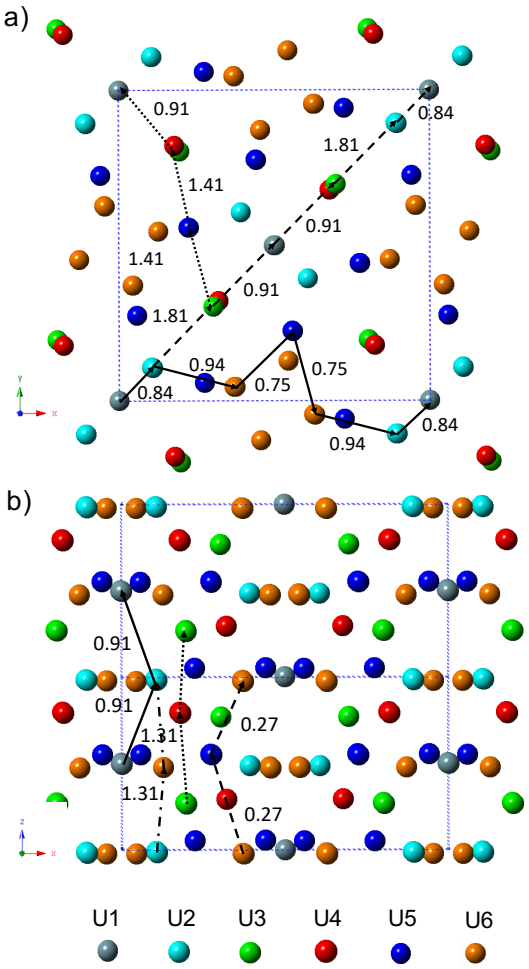

Figure 5: a) Net migration pathways for diffusion of type 1 vacancies in the x-y plane (indicated by unique dashes for each mechanism). Other vacancy types diffuse using the same mechanisms. The solid line represents the lowest energy options and corresponds to the active diffusion mechanism. b) Net migration pathways for diffusion of type 1, 2, 3 and 6 vacancies along the z axis (indicated by unique dashes for each vacancy site). The single dash line represents the pathway with lowest migration barrier and thus corresponds to the active diffusion mechanism along the z direction. In both figures, the start of the first arrow represents a vacancy, which then follows the direction of the arrows. The atoms move in the direction opposite to the arrows. The numbers refer to the barrier height with V_{U6} as the reference (in eV).

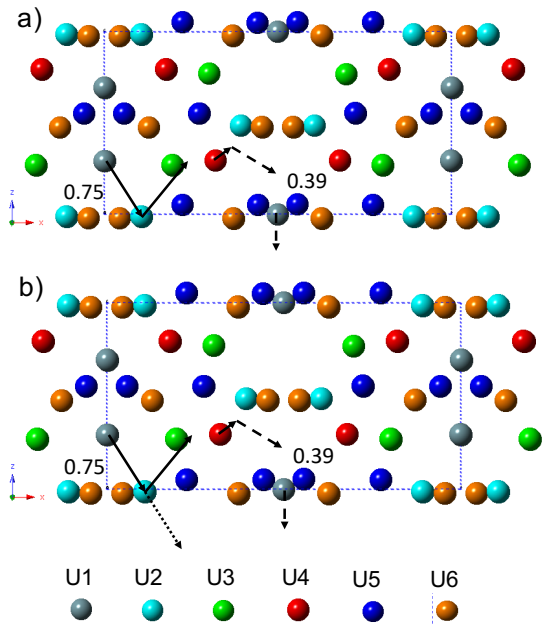

Figure 6: a) Interstitial diffusion in the x-y plane. b) Similar to a), but with the migration direction along the z axis changed for some steps such that net diffusion occurs along this axis. The difference compared a) is highlighted by the dotted arrow. The numbers refer to the barrier height with U_{i1} as the reference (in eV).

are several pathways that can lead to net diffusion with a very similar effective migration barrier would lead to a revision of the multiplicity numbers, but would not significantly change the results. The attempt frequency in the pre-exponential factor was calculated to be 6.3×10^{12} s^{-1} for the fastest vacancy mechanism in z direction using the methodology presented in Sec. 2.2. This value was used for all other diffusion mechanisms. The vacancy and interstitial diffusion rates in the x-y plane and z direction are plotted in Figure 7 for the fastest mechanisms identified in Figures 5 and 6. Vacancy diffusion in the z direction is noticeably faster than the other mechanisms, between one and two orders of magnitude depending on temperature. This difference is sufficiently large to conclude that the simplifying assumption of using a same value of the attempt frequency for all mechanisms, as derived from the fastest vacancy mechanism, is very unlikely to change the order of defect diffusivities. The interstitial diffusivities fall in between the x-y and z vacancy mechanisms.

The point defect diffusivities shown in Figure 7 are useful for analyzing radiation damage, since they control the rate of recombination and annihilation by sinks and thus the irradiation induced concentrations. However, unlike the self-diffusivity, they are not available through direct experimental measurements. The self-diffusivity for the interstitial and vacancy mechanisms are obtained by combining Eqs. 1 and 10. The parameters for the

	E_m (eV)	E_f (eV)	S_f (k_B)	ν (s^{-1})	d (Å)	Z	D_z	α
Vac. x-y	0.94	1.86	9.76	6.3×10^{12}	5.380	4	4	1/15
Vac. z	0.27	1.32	1.34	6.3×10^{12}	2.828	2	2	1/15
Int. x-y	0.75	1.49	0.35	6.3×10^{12}	7.608	4	4	1/15
Int. z	0.75	1.49	0.35	6.3×10^{12}	2.828	2	2	1/15

Table 5: Parameters for the active vacancy and interstitial diffusion mechanisms in the x-y plane and along the z direction. The parameters are defined in Eqs. 1, 8 and 10.

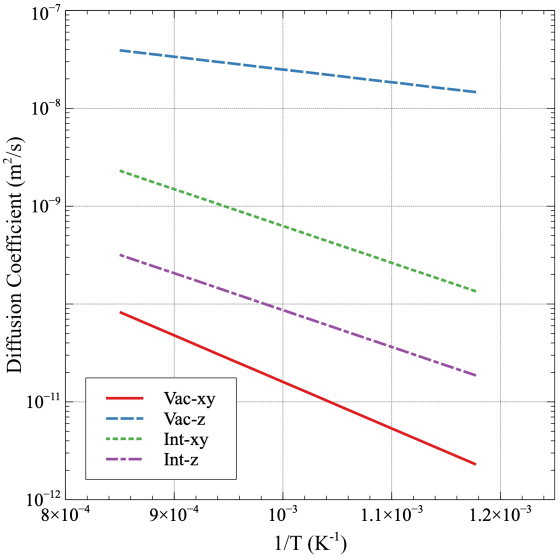

Figure 7: Vacancy and interstitial diffusivities in the x-y plane and along the z axis in β-U. Vacancy diffusion in the z direction is almost two orders of magnitude higher than the other mechanisms.

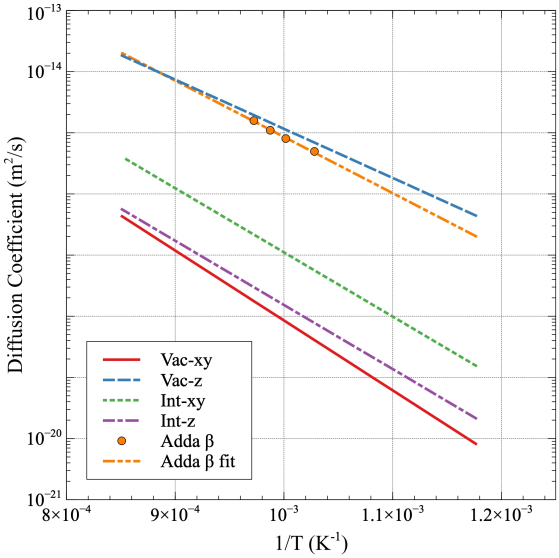

Figure 8: Uranium self-diffusivities in the x-y plane and along the z axis in β-U. All the diffusivities are similar, with exception for vacancy diffusion in the z direction, which is at least two orders of magnitude faster. The experimental data for β-U due to Adda et al. [2] is also included as reference (the squares show the measured points and the line represents the correlation derived from the data points).

diffusion mechanisms are collected in Table 5 and the results are plotted in Figure 8. This figure confirms that vacancy diffusion in the z direction is the fastest mechanism for uranium self-diffusion. The diffusion rate for this mechanism agrees well with the experimental data due to Adda et al. [2]. The slope of the Arrhenius curve is slightly different between calculations and experiments (0.2 eV), which is still considered satisfactory agreement. The deviation from a linear relation in the experimental data points is sufficient to claim that the 0.2 eV is within the range of uncertainty. The results confirm that the self-diffusivity in the β-U phase is lower than in both the high-temperature γ-U [3] and the low temperature α-U [1] phases (not shown in Figure 8).

4. Conclusions

The thermodynamic and kinetic properties of point defects in β-U were calculated from Density Functional Theory (DFT). The defect formation energies and entropies provide estimates of defect concentrations in thermal equilibrium, which predict the U1 vacancy to dominate. The stability of this vacancy is driven by a high formation entropy, while U5 and U6 vacancies actually have lower formation energies. Interstitials are found to be lower in concentration than vacancies, similar to α-U, but in contrast to γ-U. The highest concentration defect is a split interstitial along the z axis involving the U1 atom. The fastest diffusion mechanism refers to a U6 vacancy in the z direction, which is between one and two orders of magnitude faster than

any of the other mechanisms depending on temperature. The predicted self-diffusivity for this mechanism agrees very well with available experimental self-diffusivities.

Acknowledgements

This work was sponsored by the Nuclear Energy Advanced Modeling and Simulation (NEAMS) program under the US Department of Energy. Los Alamos National Laboratory, an affirmative action/equal opportunity employer, is operated by Triad National Security, LLC, for the National Nuclear Security Administration of the U.S. Department of Energy under Contract No. 89233218CNA000001.

[1] M. Stelly, J. Servant, Coefficient de diffusion du fer dans l'uranium en phase α a 645°C, J. Nucl. Mater. 43 (3) (1972) 269–272.

[2] H. Matvke, Diffusion processes in nuclear fuels, J. Less Common Met. 121 (1986) 537–564, proceedings of Actinides 85, Aix en Provence - Part I.

[3] Y. Adda, A. Kirianenko, Etude de l'autodiffusion de l'uranium en phase γ, J. Nucl. Mater. 1 (2) (1959) 120–126.

[4] H. Matter, J. Winter, W. Triftshäuser, Investigation of vacancy formation and phase transformations in uranium by positron annihilation, J. Nucl. Mater. 88 (2) (1980) 273–278.

[5] K. R. Lund, K. G. Lynn, M. H. Weber, M. A. Okuniewski, Vacancy Formation Enthalpy in Polycrystalline Depleted Uranium, J. Phys. Conf. Ser. 443 (2013) 012021.

[6] G.-Y. Huang, B. D. Wirth, First-principles study of diffusion of interstitial and vacancy in α U–Zr, J. Phys. Condens. Matter 23 (20) (2011) 205402.

[7] B. Beeler, C. Deo, M. Baskes, M. Okuniewski, First principles calculations of the structure and elastic constants of α, β and γ uranium, J. Nucl. Mater. 433 (1) (2013) 143–151.

[8] B. Beeler, D. Andersson, C. Jiang, Y. Zhang, Ab initio molecular dynamics investigation of point defects in γ-U, J. Nucl. Mater. 545 (2021) 152714.

[9] B. Beeler, B. Good, S. Rashkeev, C. Deo, M. Baskes, M. Okuniewski, First principles calculations for defects in U, J. Phys. Condens. Matter 22 (50) (2010) 505703.

[10] B. Beeler, C. Deo, M. Baskes, M. Okuniewski, Atomistic properties of γ uranium, J. Phys. Condens. Matter 24 (7) (2012) 075401.

[11] P. Söderlind, A. Landa, P. E. A. Turchi, Comment on "Correlation and relativistic effects in U metal and U-Zr alloy: Validation of ab initio approaches", Phys. Rev. B 90 (2014) 157101.

[12] W. Xie, W. Xiong, C. A. Marianetti, D. Morgan, Correlation and relativistic effects in U metal and U-Zr alloy: Validation of ab initio approaches, Phys. Rev. B 88 (2013) 235128.

[13] P. Söderlind, First-principles elastic and structural properties of uranium metal, Phys. Rev. B 66 (2002) 085113.

[14] J. Bouchet, F. Bottin, High-temperature and high-pressure phase transitions in uranium, Phys. Rev. B 95 (2017) 054113.

[15] I. A. Kruglov, A. Yanilkin, A. R. Oganov, P. Korotaev, Phase diagram of uranium from ab initio calculations and machine learning, Phys. Rev. B 100 (2019) 174104.

[16] A. Castellano, F. m. c. Bottin, B. Dorado, J. Bouchet, Thermodynamic stabilization of $\gamma-$U $-$ Mo alloys: Effect of Mo content and temperature, Phys. Rev. B 101 (2020) 184111.

[17] B. Beeler, B. Good, S. Rashkeev, C. Deo, M. Baskes, M. Okuniewski, First-principles calculations of the stability and incorporation of helium, xenon and krypton in uranium, J. Nucl. Mater. 425 (1) (2012) 2–7, microstructure Properties of Irradiated Materials.

[18] Y. Adda, A. Kirianenko, C. Mairy, Etude de l'autodiffusion de l'uranium en phase β, J. Nucl. Mater. 1 (3) (1959) 300–301.

[19] Y. Adda, A. Kirianenko, Abaissement des coefficients d'autodiffusion de l'uranium en phase γ par des additions de molybdene, de zirconium ou de niobium, J. Nucl. Mater. 6 (1) (1962) 135–136.

[20] J. Li, Q. Ren, C. Lu, L. Lu, Y. Dai, B. Liu, Structure, formation energies and elastic constants of uranium metal investigated by first principles calculations, J. Alloys Compd. 516 (2012) 139–143.

[21] G. Kresse, J. Hafner, Ab initio molecular dynamics for open-shell transition metals, Phys. Rev. B 48 (1993) 13115–13118.

[22] G. Kresse, J. Furthmüller, Efficiency of ab-initio total energy calculations for metals and semiconductors using a plane-wave basis set, Comp. Mater. Sci. 6 (1996) 15–50.

[23] G. Kresse, J. Furthmüller, Efficient iterative schemes for ab initio total-energy calculations using a plane-wave basis set, Phys. Rev. B 54 (1996) 11169–11186.

[24] G. Henkelman, B. P. Uberuaga, H. Jónsson, A climbing image nudged elastic band method for finding saddle points and minimum energy paths, J. Chem. Phys. 113 (22) (2000) 9901–9904.

[25] J. P. Perdew, K. Burke, M. Ernzerhof, Generalized Gradient Approximation Made Simple, Phys. Rev. Lett. 77 (1996) 3865–3868.

[26] G. Kresse, D. Joubert, From ultrasoft pseudopotentials to the projector augmented-wave method, Phys. Rev. B 59 (1999) 1758–1775.

[27] P. E. Blöchl, Projector augmented-wave method, Phys. Rev. B 50 (1994) 17953–17979.

[28] J. Donohue, H. Einspahr, The structure of β-uranium, Acta Crystallogr. B 27 (9) (1971) 1740–1743.

[29] H. J. Monkhorst, J. D. Pack, Special points for Brillouin-zone integrations, Phys. Rev. B 13 (1976) 5188–5192.

[30] Y. Mishin, M. R. Sørensen, A. F. Voter, Calculation of point-defect entropy in metals, Phil. Mag. A 81 (11) (2001) 2591–2612.

[31] G. Henkelman, B. P. Uberuaga, H. Jonsson, A climbing image nudged elastic band method for finding saddle points and minimum energy paths, J. Chem. Phys. 113 (2000) 9901.

[32] G. H. Vineyard, Frequency factors and isotope effects in solid state rate processes, J. Phys. Chem. Solids 3 (1957) 121–127.